

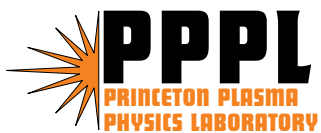
PPPL-4026

PPPL-4026

The Effect on Stellarator Neoclassical Transport of a Fluctuating Electrostatic Spectrum

H.E. Mynick and A.H. Boozer

November 2004



PPPL Report Disclaimers

Full Legal Disclaimer

This report was prepared as an account of work sponsored by an agency of the United States Government. Neither the United States Government nor any agency thereof, nor any of their employees, nor any of their contractors, subcontractors or their employees, makes any warranty, express or implied, or assumes any legal liability or responsibility for the accuracy, completeness, or any third party's use or the results of such use of any information, apparatus, product, or process disclosed, or represents that its use would not infringe privately owned rights. Reference herein to any specific commercial product, process, or service by trade name, trademark, manufacturer, or otherwise, does not necessarily constitute or imply its endorsement, recommendation, or favoring by the United States Government or any agency thereof or its contractors or subcontractors. The views and opinions of authors expressed herein do not necessarily state or reflect those of the United States Government or any agency thereof.

Trademark Disclaimer

Reference herein to any specific commercial product, process, or service by trade name, trademark, manufacturer, or otherwise, does not necessarily constitute or imply its endorsement, recommendation, or favoring by the United States Government or any agency thereof or its contractors or subcontractors.

PPPL Report Availability

This report is posted on the U.S. Department of Energy's Princeton Plasma Physics Laboratory Publications and Reports web site in Fiscal Year 2005. The home page for PPPL Reports and Publications is: http://www.pppl.gov/pub_report/

Office of Scientific and Technical Information (OSTI):

Available electronically at: <http://www.osti.gov/bridge>.

Available for a processing fee to U.S. Department of Energy and its contractors, in paper from:

U.S. Department of Energy
Office of Scientific and Technical Information
P.O. Box 62
Oak Ridge, TN 37831-0062
Telephone: (865) 576-8401
Fax: (865) 576-5728
E-mail: reports@adonis.osti.gov

National Technical Information Service (NTIS):

This report is available for sale to the general public from:

U.S. Department of Commerce
National Technical Information Service
5285 Port Royal Road
Springfield, VA 22161
Telephone: (800) 553-6847
Fax: (703) 605-6900
Email: orders@ntis.fedworld.gov
Online ordering: <http://www.ntis.gov/ordering.htm>

The effect on stellarator neoclassical transport of a fluctuating electrostatic spectrum

H.E. Mynick^a and A.H. Boozer^b

^aPlasma Physics Laboratory, Princeton University

^bDept. of Applied Physics & Mathematics, Columbia University

Abstract

We study the effect on neoclassical transport of applying a fluctuating electrostatic spectrum, such as produced either by plasma turbulence, or imposed externally. For tokamaks, it is usually assumed that the neoclassical and “anomalous” contributions to the transport roughly superpose, $D = D_{nc} + D_{an}$, an intuition also used in modeling stellarators. An alternate intuition, however, is one where it is the collisional and anomalous *scattering frequencies* which superpose, $\nu_{ef} = \nu + \nu_{an}$. For nonaxisymmetric systems, in regimes where $\partial D / \partial \nu < 0$, this “ ν_{ef} picture” implies that turning on the fluctuations can *decrease* the total radial transport. Using numerical and analytic means, it is found that the total transport has contributions conforming to each of these intuitions, either of which can dominate. In particular, for stellarators, the ν_{ef} picture is often valid, producing transport behavior differing from tokamaks.

PACS #s: 52.55.Dy, 52.55.Hc, 52.35.Ra

I. Introduction

In this paper, we examine the effect on neoclassical transport in a stellarator or tokamak of introducing an additional fluctuating electrostatic (ES) field, such as that produced by plasma drift turbulence, or imposed externally. The theory of neoclassical transport in tokamaks (*e.g.*, Refs. 1–3) and stellarators (*e.g.*, Refs. 4,5) has been extensively developed. Much theoretical work has also been done on turbulent transport, mainly in tokamaks (see, *e.g.*, Ref. 6). With increasing interest in stellarators in recent years, some studies of turbulent transport in stellarators (*e.g.*, Refs. 7–10) have been carried out, though the greater geometric complexity of stellarators has made numerical and analytic progress more difficult than for tokamaks.

Here, we address two general intuitions in the literature about what one expects the effect of the additional ES spectrum should be. The first, probably derived principally from tokamak studies, here termed the “additive picture”, is that the contributions to radial transport from Coulomb collisions and from the fluctuating spectrum are roughly independent, so that the total radial transport coefficient D may be approximately written $D \simeq D_{nc} + D_{an}$, with the usual Coulomb collisionality (ν) producing neoclassical transport (D_{nc}), and the fluctuations producing the “anomalous” contribution (D_{an}). This same view has been applied in modeling stellarators (*e.g.*, Refs. 11–14), supported in part by the observation¹⁵ that stellarator empirical scaling laws are similar to ones originally developed for tokamaks, such as Lackner-Gottardi scaling.¹⁶

On the other hand, one may regard the ES fluctuations as an additional source of collisionality, so that the total effective velocity-space scattering frequency ν_{ef} may be written as the sum of the Coulomb collisionality plus that from the fluctuations, $\nu_{ef} = \nu + \nu_{an}$. Thus, within this “ ν_{ef} picture”, a simple guess for the effect

of the fluctuations is to replace ν by ν_{ef} in $D_{nc}(\nu)$. In an axisymmetric tokamak, where D_{nc} increases with increasing collisionality ($\partial D/\partial\nu > 0$), the additive and ν_{ef} pictures are consistent, at least qualitatively. However, in stellarators, or rippled tokamaks, there are regimes of collisionality in which $\partial D/\partial\nu < 0$, so that the ν_{ef} intuition would predict that increasing the fluctuation amplitude should *decrease* radial transport, opposite the additive expectation. The present work addresses to what extent these expectations hold, using both numerical and analytical methods.

The idea that ES fluctuations might provide an effective collisionality was discussed in Refs. 17,18, and experimentally tested on the Saturn stellarator¹⁹ to enhance the plasma confinement time (by about 40%), by applying an RF electric field with frequency ω comparable to the bounce frequency Ω_{be} of electrons trapped in a helical ripple well in order to enhance their detrapping rate. More recently, Shishkin and coworkers have proposed applications of this idea, *e.g.*, detrapping electrons to control the radial electric field,²⁰ and entrapping ions to enhance impurity removal.^{21,22} Thus, the additive intuition derives principally from modeling internally-generated fluctuations, while the ν_{ef} intuition derives from externally-imposed fluctuations, though the two are different cases of the same phenomenon. Here, we present numerical results and an analytic framework exhibiting both types of behavior.

The remainder of the paper is organized as follows. In Sec. II, we set up the framework for the calculations to follow, introducing some notation, the model to be used, and the numerical approach employed. A first series of numerical results is presented in Sec. III, finding situations where the ν_{ef} picture is valid and substantial (order unity), and others where it is relatively small. To gain a better understanding of the dependencies found, in Sec. IV we turn to a theoretical analysis of the issue. The numerical results of Sec. III are for distributions f distributed “globally” over

a flux surface and in pitch. The analytic results in Sec. IV provide more detailed information, coming from distributions more localized in flux surface launch point and in pitch. In Sec. V, we provide a comparison of the analytic results and a second set of numerical runs which are also of this more localized nature. We find rough agreement between the detailed analytic and numerical results. We also find agreement between ν_{an}/ν computed analytically and numerically, and from the analytic expression for this ratio obtain a prediction for the modification by the fluctuations of D_{nc} which agrees with the global numerical results of Sec. III. In Sec. VI we summarize our findings, and discuss some of their implications.

II. Preliminaries

We study 3 toroidal configurations, all related to the design for the NCSX quasi-axisymmetric (QA) stellarator, currently under construction.¹³ The first configuration, designated QA1, is one variant of the LI383 design for NCSX. The second, designated TOK1, is the tokamak resulting from dropping all the $n \neq 0$ Fourier amplitudes B_{mn} of magnetic field strength $B \equiv |\mathbf{B}|$ in QA1. Finally, we add to the Fourier decomposition of TOK1 a single helical amplitude $B_{m_0 n_0}$, of size considerably greater than the $n \neq 0$ amplitudes in QA1, resulting in a model conventional stellarator CS1. (We take $m_0 = 2, n_0 = 6$, and ripple amplitude $\delta = 7.5\%$ halfway out, compared with an effective δ of less than 1% for NCSX.) These configurations are characterized in Fig. 1, which shows for each, on the left, a contour plot of $B(\theta, \zeta)$ over a flux surface, and on the right, B along a field line, for one poloidal transit. Here, θ, ζ are the poloidal and toroidal flux coordinates, respectively. In terms of these, along with the toroidal flux $2\pi\psi$ and poloidal flux $2\pi\psi_p$, the magnetic field $\mathbf{B}(\mathbf{x})$ may be written in the contravariant (Clebsch)

representation

$$\mathbf{B} = \nabla\psi \times \nabla\theta + \nabla\zeta \times \nabla\psi_p = \nabla\alpha \times \nabla\psi_p, \quad (1)$$

where $\alpha \equiv \zeta - q\theta$, and $\iota \equiv q^{-1} \equiv d\psi_p/d\psi$ is the rotational transform.

On these magnetic fields we superpose a time-independent radial ambipolar electric field $E_r \equiv -\partial_r\Phi_0$, with ambipolar potential $\Phi_0(\psi) = \alpha_E(1 - \psi/\psi_a) = \alpha_E(1 - r^2/a^2)$, where α_E is a scaling amplitude, ψ_a is ψ at the plasma edge, a is the value of r at $\psi = \psi_a$, and we define an average minor radius $r(\psi)$ with units of length by $\psi \equiv B_0 r^2/2$, with B_0 the average magnetic field strength on axis. All 3 configurations have $B_0 = 30$ kG, and average major radius $R_0 \equiv R(\psi = 0, \theta = 0, \zeta = 0) = 100$ cm.

To these equilibrium fields, we add a fluctuating spectrum of electrostatic perturbations $\delta\phi(\mathbf{x}, t) = \sum_{\mathbf{m}} \phi_{\mathbf{m}}(\psi) \cos(\eta_{\mathbf{m}} - \omega_{\mathbf{m}}t)$, where $\mathbf{m} \equiv (m, n)$ is a vector index labeling the modes, $\eta_{\mathbf{m}} \equiv n\zeta - m\theta + \eta_{\mathbf{m}0}$, $\omega_{\mathbf{m}}$ is the mode frequency, and $\phi_{\mathbf{m}}(\psi)$ is the mode amplitude. It is given by $e\phi_{\mathbf{m}}/E_1 = \hat{a}_{\mathbf{m}}A_{\mathbf{m}}(\psi)$, where e is the particle charge, E_1 a reference energy, here taken equal 1 keV, $A_{\mathbf{m}}(\psi)$ gives the mode radial variation, with maximum 1, and $\hat{a}_{\mathbf{m}}$ is the mode amplitude. To model drift turbulence, we take mode frequencies given by $\omega_{\mathbf{m}} = \alpha_{\omega}\omega_{*k}/(1 + k_{\perp}^2\rho_g^2)$, and amplitudes given by $\hat{a}_{\mathbf{m}} = 10^{-3}\alpha_A/(1 + k_{\perp}^2\rho_g^2)$, with α_{ω} and α_A scaling amplitudes. Here, $\omega_{*k} \equiv -k_{\theta}\kappa_n cT/(eB)$ is the diamagnetic frequency, with $\kappa_n \equiv -\partial_r(\ln n_0)$, and $\partial_r \equiv \partial/\partial r$ denotes a partial derivative.

We will consider 2 spectra. The first, denoted S1, models drift turbulence. Such modes tend to keep k_{\parallel} small, hence to peak near rational surfaces with $q(\psi) \sim q_{mn} \equiv m/n$. The 3 configurations here have q in the range $q_0 = 2.53 \simeq 5/2$ at $\psi = 0$, and $q_a = 1.51 \simeq 3/2$ at $\psi = \psi_a$. We thus take \mathbf{m} having low m, n , with $q_{\mathbf{m}}$ in this range. We choose the 6 modes $m/n = \{3/2, 5/3, 2/1, 4/2, 6/3, 5/2\}$. For these parameters, hydrogen ions at $r = a/2$ with energy $E = E_1$ have

$k_{\perp}\rho_g \simeq .035m$, putting this parameter in the range .07–.21 for the m -values used, at or slightly below typical observed values ($\langle k_{\perp}\rho_g \rangle \sim 0.3$) for ITG turbulence in tokamaks.

For the second spectrum, denoted S2, we take the same model as S1, but with all the n -values in S1 set to zero. This yields larger k_{\parallel} , hence larger parallel electric fields E_{\parallel} , such as were taken in the Saturn experiment in Ref. 19, in order to most effectively break the bounce action J_b , and thereby enhance the ν_{ef} effect.

For numerical investigation we use the ORBIT guiding-center code,²³ which is able to conveniently read numerical equilibria. For speed, and because it captures the essential physics, we launch monoenergetic ensembles, of N_p particles at $\psi_0/\psi_a = 0.5$, and compute the radial diffusion coefficient D from $D = \langle (\delta r_i)^2 / (2\tau_i) \rangle$, where $\langle F \rangle \equiv N_p^{-1} \sum_i F_i$ is an average over all N_p particles, $\delta r_i \equiv r_i - \langle r \rangle$, and τ_i is the run time for particle i , the smaller of its confinement time and a maximum run time T allowed for the ensemble. With this definition, in situations (such as at very low collisionality ν and small E_r) where the particle loss becomes non-diffusive, this prescription for D still provides a meaningful measure of the transport, an average inverse confinement time.

The code uses the numerical counterpart²⁴ of the Lorentz collision operator C_L ,

$$C_L f = \frac{\nu v_{\parallel}}{B} \partial_{\mu} M v_{\parallel} \partial_{\mu} f = \frac{\nu}{2} \partial_{\lambda} (1 - \lambda^2) \partial_{\lambda} f, \quad (2)$$

with $\mu = M v_{\perp}^2 / (2B)$ the particle magnetic moment, and $\lambda = v_{\parallel} / v$ the particle pitch. C_L conserves particles and energy. The code works in units where $R_0 = M = \Omega_{g0} = 1$, with M the particle mass and $\Omega_{g0} \equiv eB_0 / (Mc)$. In these units, energy $E_1 = \frac{1}{2}(\rho_g/R_0)^2 \simeq 3.88 \times 10^{-6}$, hence $\rho_g/R_0 \simeq 2.79 \times 10^{-3}$.

III. Numerical Results

We first look at transport for spectrum S1, modeling drift turbulence, with $E_r = 0$. This small value of E_r means that the ions are in the $1/\nu$ regime of the “superbanana branch” of transport, a situation which usually holds in a real experiment for electrons. The $E_r = 0$ ion results given here thus also provide a picture of what may be expected for the analogous effect for electrons. In Fig. 2 is shown a scan of radial diffusion coefficient D versus central electron density n_{e0} (and thus ν), with the fluctuations turned off ($\alpha_A = 0$), for each of TOK1, QA1, and CS1. We use monoenergetic ensembles of $N_p = 3000$ particles, randomly distributed in θ, ζ , and λ . For TOK1 (bottom curve), one notes the banana regime at low- ν , starting to bend over into the plateau regime at the highest ν . Just above this is the transport from QA1, close to that from TOK1 at high- ν , and manifesting a weak $1/\nu$ -regime as one descends from there toward lower ν . Well above that is the transport from CS1, showing a much stronger $1/\nu$ regime, as one would expect. In the flattened part of this curve at lowest ν , the transport is no longer primarily diffusive, dominated by helically-trapped particles (trapping state index $\tau = h$) walking directly to the machine wall. (We will also designate toroidally-trapped particles by $\tau = t$, and passing particles by $\tau = p$.)

In Fig. 3 we turn on the fluctuations, showing a scan of D versus α_A , at $\alpha_\omega = 0.03$ and $n_{e0} = 10^{13}/\text{cm}^3$. From Fig. 2, this value of n_{e0} places CS1 just below its descent into the $1/\nu$ regime, where one might expect a disparity between the additive and ν_{ef} pictures to appear. As defined in Sec. II, $\alpha_A = 10$ corresponds to $e\phi_m/E_1 \simeq 10^{-2}$ at the point of maximum amplitude of ϕ_m , typical of drift turbulence. In Fig. 3b, the simple neoclassical ($\alpha_A = 0$) values are subtracted from the full D shown in Fig. 3a, to show the anomalous increment D_{an} above neoclassical. In either figure, one notes the monotonic increase with α_A of D

for TOK1, roughly quadratic in form, and consistent with the additive intuition generally accepted for tokamak transport. The QA1 curve roughly parallels the TOK1 curve, but has a modest amount of oscillatory structure on top of this. The CS1 curve (lying above the shown range in Fig. 3a) displays much more of this structure, so that over this range it is not clear that on average D is increasing with α_A at all.

In Fig. 4 is shown a scan in frequency amplitude α_ω , at $n_{e0} = 10^{13}/\text{cm}^3$ and $\alpha_A = 10$. As for Fig. 3, Fig. 4a shows the total transport $D = D_{nc} + D_{an}$, and Fig. 4b shows the anomalous increment D_{an} alone. The TOK1 curve displays a sizeable peak at small frequencies, of half-width $\delta\alpha_\omega \simeq 0.03$, with D falling off monotonically away from that peak toward the neoclassical value. From comparison of the mode and particle frequencies, this appears to be due to a resonance of mode frequencies with the bounce time of $\tau = t$ particles. As in Fig. 3, the QA1 and CS1 stellarator curves are nonmonotonic, having an additional oscillatory structure at larger frequencies, of amplitude much larger for CS1, as one expects. In CS1, the central “tokamak peak” visible in the TOK1 curve is still evident, and the additional structure shows a succession of peaks spaced at roughly $\Delta\alpha_\omega \simeq 0.08$. One notes that this additional structure in both QA1 and CS1 makes D_{an} *negative* for some α_ω , counter to the additive picture, and consistent with the ν_{ef} picture.

While $D_{an} < 0$ in the above results is conceptually interesting, it is only a small effect, inducing a peak-to-peak change of around 8%. This is in part because we have thus far taken $E_r = \alpha_E = 0$, making D_{nc} very large for ions in CS1, and also because, as noted earlier, spectrum S1 provides a relatively small $E_{||}$ for inducing turbulent pitch-angle scattering. Therefore, we now compare the effects of spectrum S2 versus S1, and of $\alpha_E = 0$ versus $\alpha_E = 0.6$, a value large enough

to close the superbanana orbits, *i.e.*, to make $\tau = h$ particles confined instead of walking directly out of the machine. We also henceforth focus on CS1, for which these effects are more pronounced.

In Fig. 5 we show a scan of D versus density for CS1, showing the neoclassical transport ($\alpha_A = 0$) for $\alpha_E = 0$ (upper curve) and $\alpha_E = 0.6$ (lower). The $1/\nu$ regime is again evident for $\alpha_E = 0$. The $\alpha_E = 0.6$ curve displays 2 collisionality regimes, the $1/\nu$ regime at higher ν , having $\partial D/\partial \nu < 0$, and at lower ν , the “superbanana regime”,^{4,25} for which $\partial D/\partial \nu > 0$. If the ν_{ef} picture were correct, this change in sign in $\partial D/\partial \nu$ should cause a corresponding sign change in the increment D_{an} to D when the spectrum is turned on.

This expectation is borne out in Fig. 6, which shows 4 frequency scans, each for $n_{e0} = 10^{13}/\text{cm}^3$ and $\alpha_A = 10$, as in Fig. 4. As before, Fig. 6a shows the full D , and Fig. 6b shows D_{an} . One notes the central tokamak peak in each curve, though in the 2 $\alpha_E = 0.6$ curves C and D the peak is displaced toward more negative α_ω than the $\alpha_E = 0$ curves A and B, a result of the $E \times B$ drifts of trapped particles. Comparing curves A and B, one sees that spectrum S2 induces a far larger effect, producing a reduction in D of about 30% around $|\alpha_\omega| \simeq 0.22$, excluding the central tokamak peak.

Comparing the $\alpha_E = 0.6$ curves C and D, one again sees that S2 induces a much larger effect, again maximum around $|\alpha_\omega| \simeq 0.22$, but in this case the anomalous increment D_{an} is *positive*, as one would expect from the ν_{ef} picture.

IV. Theory

We now explore this effect analytically. To study it, we employ the “action-angle formalism,” originally formulated for tokamaks by Kaufman.²⁶ In this formalism, one parametrizes the 6-dimensional phase space \mathbf{z} with the 3 invariant

actions \mathbf{J} of the unperturbed motion and their 3 conjugate angles $\boldsymbol{\theta}$, and considers the diffusion in \mathbf{J} -space under the influence of some perturbation, either collisions or a fluctuating spectrum. The angle-averaged distribution $f(\mathbf{J})$ is then governed by a kinetic equation

$$\partial_t f = Cf = \partial_{\mathbf{J}} \cdot \mathbf{D} \cdot \partial_{\mathbf{J}} f, \quad (3)$$

with $\partial_{\mathbf{J}}$ denoting a gradient in \mathbf{J} -space.

The Hamiltonian governing the collisionless motion has an unperturbed and perturbing part, $H(\mathbf{z}) = H_0(\mathbf{J}) + h(\mathbf{z})$, where $h \equiv e\delta\phi(\mathbf{x}, t) = \sum_{\mathbf{m}} e\phi_{\mathbf{m}}(\psi) \cos(\eta_{\mathbf{m}} - \omega_{\mathbf{m}}t)$. From Hamilton's equations, one has

$$\dot{\boldsymbol{\theta}} = \partial_{\mathbf{J}} H = \boldsymbol{\Omega}(\mathbf{J}) + \partial_{\mathbf{J}} h \simeq \boldsymbol{\Omega}(\mathbf{J}), \quad (4)$$

$$\dot{\mathbf{J}} = -\partial_{\boldsymbol{\theta}} h = -i \sum_{\mathbf{l}, \mathbf{m}} \mathbf{l} h_{\mathbf{l}\mathbf{m}}(\mathbf{J}) \exp(i\mathbf{l} \cdot \boldsymbol{\theta} - i\omega_{\mathbf{m}}t), \quad (5)$$

where $\boldsymbol{\Omega}(\mathbf{J}) \equiv \partial_{\mathbf{J}} H_0$, and \mathbf{l} is the 3-component vector index of the ‘‘coupling coefficients’’ $h_{\mathbf{l}\mathbf{m}}(\mathbf{J})$, the Fourier amplitudes of perturbing Hamiltonian $h(\boldsymbol{\theta}, \mathbf{J}) = \sum_{\mathbf{m}} h_{\mathbf{m}}(\boldsymbol{\theta}, \mathbf{J})$. From these equations, one obtains²⁶ the quasilinear diffusion tensor $\mathbf{D}_{an}(\mathbf{J})$ describing the diffusion in \mathbf{J} -space induced by h ,

$$\mathbf{D}_{an}(\mathbf{J}) = \sum_{\mathbf{l}, \mathbf{m}} \mathbf{l} \pi \delta(\mathbf{l} \cdot \boldsymbol{\Omega} - \omega_{\mathbf{m}}) |h_{\mathbf{l}\mathbf{m}}|^2, \quad (6)$$

structurally the same as the usual expression for the quasilinear diffusion tensor in momentum space $\mathbf{p} \equiv M\mathbf{v}$ for an unmagnetized plasma, which Eq.(6) generalizes to any configuration where the unperturbed motion is integrable. The particular choice of $(\boldsymbol{\theta}, \mathbf{J})$ depends upon the geometry studied. For the present case, an appropriate choice is $\boldsymbol{\theta} = (\theta_g, \theta_b, \bar{\alpha})$, $\mathbf{J} = (J_g, J_b, J_d \equiv (e/c)\bar{\psi}_p)$, with $J_g \equiv (Mc/e)\mu$ the gyroaction, θ_g the gyrophase, describing the fastest time scale of the motion, J_b the bounce action, θ_b its conjugate bounce phase, $\bar{\psi}_p$ the drift-orbit averaged value of ψ_p , and its conjugate phase $\bar{\alpha}$, the orbit-averaged Clebsch

coordinate α , describing the slow, drift time-scale. Correspondingly one has the characteristic frequencies of motion $\boldsymbol{\Omega} \equiv (\Omega_g, \Omega_b, \Omega_d)$, with gyrofrequency Ω_g , bounce frequency Ω_b , and drift frequency Ω_d , and vector index $\mathbf{l} \equiv (l_g, l_b, l_d)$, with gyro- and bounce-harmonics $l_{g,b} = 0, \pm 1, \pm 2, \dots$, and drift index l_d , evaluated below. \mathbf{J} -space thus has 2 velocity-like actions J_g, J_b , and one space-like one, J_d .

To extract physical information from Eq.(6), it will be useful to take projections of \mathbf{D} in various \mathbf{J} -space directions. We define the (contravariant) basis vectors $\boldsymbol{\epsilon}^i \equiv \partial_{\mathbf{J}} J_i, (i = g, b, d)$, and for any function $F(\mathbf{J})$, we also define $\boldsymbol{\epsilon}^F \equiv \partial_{\mathbf{J}} F$. Thus, for $F \rightarrow E$, one has $\boldsymbol{\epsilon}^E \equiv \partial_{\mathbf{J}} H_0 \equiv \boldsymbol{\Omega}$. In the comparisons in Sec. V, we shall be principally interested in 3 ‘‘diagonal’’ projections of Eq.(6),

$$\begin{aligned} D^{rr} &\equiv \boldsymbol{\epsilon}^r \cdot \mathbf{D} \cdot \boldsymbol{\epsilon}^r = \sum_{\mathbf{l}, \mathbf{m}} (l_d B_0 r / q)^2 \pi \delta(\mathbf{l} \cdot \boldsymbol{\Omega} - \omega_{\mathbf{m}}) |h_{\mathbf{l}\mathbf{m}}|^2, \\ D^{EE} &\equiv \boldsymbol{\epsilon}^E \cdot \mathbf{D} \cdot \boldsymbol{\epsilon}^E = \sum_{\mathbf{l}, \mathbf{m}} \omega_{\mathbf{m}}^2 \pi \delta(\mathbf{l} \cdot \boldsymbol{\Omega} - \omega_{\mathbf{m}}) |h_{\mathbf{l}\mathbf{m}}|^2, \text{ and} \\ D^{JJ} &\equiv \boldsymbol{\epsilon}^{J_b} \cdot \mathbf{D} \cdot \boldsymbol{\epsilon}^{J_b} = \sum_{\mathbf{l}, \mathbf{m}} l_b^2 \pi \delta(\mathbf{l} \cdot \boldsymbol{\Omega} - \omega_{\mathbf{m}}) |h_{\mathbf{l}\mathbf{m}}|^2. \end{aligned}$$

We note that D^{rr} here does not represent the total radial transport computed in Sec. III, but only the ‘‘direct’’ contribution, due to the radial excursions produced by the perturbing potential. It does not account for the ‘‘indirect’’ contribution, due to modification of the velocity-space distribution by ν_{ef} , which is described by coefficients D^{EE} and D^{JJ} , and for the frequencies applied is significant mainly for particles with $\tau = h$. For such frequencies in tokamaks, which have no $\tau = h$ particles, D^{rr} should dominate. For stellarators with appreciable ripple, such as the CS1 results shown in Fig. 6, the incremental indirect contribution from ν_{an} can dominate.

For collisional transport, on the right side of Eq.(3) one instead uses for C the angle-averaged Landau operator, or a simplified form such as the angle-average \bar{C}_L of the Lorentz operator in Eq.(2). Applied to tokamaks, the action-angle framework has been used^{28,29} to compute tokamak neoclassical transport coefficients.

To treat a case having both collisions and a fluctuating spectrum, one may take $C = C_{nc} + C_{an}$ in Eq.(3), with $C_{nc} \rightarrow \bar{C}_L$. This somewhat simplifies the correct form — expression (6) should be collisionally broadened. Here, we will use only the collisionless analytic form (6), and the corresponding simulations to follow will be with the spectrum on and collisions off.

We now evaluate analytic expression (6), and in Sec. V compare its predictions with numerical results. To evaluate the coupling coefficients, we write an approximate description of the position $\mathbf{x}(\mathbf{z})$ of $\tau = h$ particles, making explicit its dependence on θ , analogous to previous tokamak applications of this formalism^{27,29}:

$$\begin{aligned}\psi &\simeq \bar{\psi} + \psi_d \cos \theta_d + \psi_2 \cos \theta_b + \psi_1 \cos \theta_g, \\ \theta &\simeq \theta_d + \theta_2 \sin \theta_b + \theta_1 \sin \theta_g, \\ \zeta &\simeq \zeta_d + \zeta_2 \sin \theta_b + \zeta_1 \sin \theta_g\end{aligned}$$

Here, the drift motion in a ripple well is described by $\theta_d(\bar{\alpha})$ and $\zeta_d(\bar{\alpha}) = \zeta_{d0} + q_{mn0}\theta_d$, with $q_{mn0} \equiv m_0/n_0$, and by “superbanana width” excursion ψ_d in ψ . The bounce motion in that well makes ψ, θ, ζ excursions ψ_2, θ_2 and $\zeta_2 \simeq q\theta_2$, and the gyromotion makes gyro-excursions ψ_1, θ_1 and ζ_1 . For simplicity, we neglect the radial variation of mode amplitude $\phi_{\mathbf{m}}(\psi)$ over the excursions ψ_d, ψ_2 , and ψ_1 . Mode phase $\eta_{\mathbf{m}}$ may be written $\eta_{\mathbf{m}} = \eta_d + z_b \sin \theta_b + z_g \sin \theta_g$, with $\eta_d \equiv n\zeta_d - m\theta_d = n\zeta_{d0} + (nq_{mn0} - m)\theta_d$, $z_b \equiv n\zeta_2 - m\theta_2 \simeq (nq - m)\theta_2$, and $z_g \equiv n\zeta_1 - m\theta_1 \simeq k_\theta \rho_g$. Putting these into the expression for $h = \sum_{\mathbf{m}} h_{\mathbf{m}}$ and using the identity $\exp(iz \sin \theta) = \sum_{l=-\infty}^{\infty} J_l(z) \exp(il\theta)$, one reads off the coupling coefficients:

$$h_{\mathbf{l}\mathbf{m}}(\mathbf{J}) = \frac{1}{2} e \bar{\phi}_{\mathbf{m}} \delta_{l_d, k_d} J_{l_g} J_{l_b}, \quad (7)$$

with $\bar{\phi}_{\mathbf{m}} \equiv \phi_{\mathbf{m}}(\bar{\psi})$, $\delta_{l,k}$ the Kronecker delta, and $k_d \equiv \partial\eta/\partial\alpha|_{\eta_0} = n(1 -$

$q_{mn}/q_{mn0})/(1 - q/q_{mn0})$ giving the (linear) transformation between η_d and $\bar{\alpha}$ at constant ripple phase $\eta_0 \equiv n_0\zeta - m_0\theta$. Here, J_{l_g} has argument z_g , J_{l_b} has argument z_b , and mode index \mathbf{m} is implicit in the definitions of $z_{g,b}$.

We perform the summation over \mathbf{l} in Eq.(6). The factor δ_{l_d,k_d} in (7) yields a single term with $l_d = k_d$ in \sum_{l_d} . Thus the term $l_d\Omega_d$ in the resonance argument $\mathbf{l} \cdot \boldsymbol{\Omega} - \omega_{\mathbf{m}}$ in (6) becomes $k_d\Omega_d = \dot{\eta}_d = (nq_{mn0} - m)\dot{\theta}_d$, and the resonance condition may be written $\omega_{\mathbf{m}} = \dot{\eta}_d + l_b\Omega_b + l_g\Omega_g$. Because $\{\Omega_b, \dot{\eta}_d, \omega_{\mathbf{m}}\} \ll \Omega_g$ and $z_g \lesssim 1$, only the $l_g = 0$ term survives the \sum_{l_g} . The resonance condition in the final \sum_{l_b} sets the value of l_b , to $\bar{l}_b \equiv [(\omega_{\mathbf{m}} - \dot{\eta}_d)/\Omega_b]$, where $[l]$ means the integer part of l . The sum over l_b has been done approximately by converting the sum to an integral, which introduces some uncertainty in the overall coefficient. Eq.(6) then yields

$$\mathbf{D}_{an}(\mathbf{J}) = \sum_{\mathbf{m}} \bar{\Pi}(\pi/4\Omega_b) |e\bar{\phi}_{\mathbf{m}}|^2 J_0^2(z_g) J_{\bar{l}_b}^2(z_b), \quad (8)$$

where $\bar{\mathbf{l}} = (k_d, \bar{l}_b, 0)$. From this one notes that $D^{ij} \equiv \boldsymbol{\epsilon}^i \cdot \mathbf{D} \cdot \boldsymbol{\epsilon}^j$ has only 4 nonzero elements, and because $D^{ij} = D^{ji}$, only 3 independent ones.

V. Analytic and Numerical Comparison

We now evaluate the elements D^{rr} , D^{EE} , and D^{JJ} analytically from Eqs.(8) and (10) (which give C_{an} and C_{nc} , respectively), and also numerically, and compare the analytic and numerical results. We also use these to compute ν_{ef}/ν , and from this, to understand the more global (in θ and λ) numerical results of Sec. III. We have described the numerical prescription for computing D^{rr} in Sec. II. Since the particle energy $E = H(\mathbf{z})$ is known at each point along an orbit, the prescription for D^{EE} is completely analogous. Computing D^{JJ} is somewhat more difficult, since it involves first computing $J_b \equiv (2\pi)^{-1} \oint d\ell M v_{\parallel}$ at each point along the orbit. (Here ℓ is the arc length along the field line the particle is on.)

Moreover, when detrapping or retrapping occurs, there is a large discontinuous jump in J_b by this definition, and a calculation of D^{JJ} loses its significance. In this work, the main focus is on $\tau = h$ particles, since these are the ones producing the superbanana transport. We accordingly compute $D^{JJ} = \langle \delta J_{bi}^2 / (2\tau_i) \rangle$ for $\tau = h$ particles, setting the run time τ_i of particle i to the smaller of total run time T and its detrapping time, analogous to the manner in which τ_i was set for computing D^{rr} . The signature indication of this process being truly diffusive, that $\langle \delta J_{bi}^2 \rangle(t) \propto t$, is still met, but with less accuracy than for D^{rr} . And while the particles here are launched with a single value of \mathbf{J} to compare with the local analytic result (8), \mathbf{J} broadens over the course of the measurement, along with the particle ψ and well-depth, thus averaging over these variables. The phase mixing needed for the numerical measurement is aided, however, by taking random initial mode phases for each particle, rather than just from mixing from the particle initial conditions, which sufficed for the global results of Sec. III.

In v_{\parallel} in the above definition for J_b , one may separate out the η_0 -dependent part of B , writing $B = B_t(\psi, \theta) + 2\delta B_0 \sin^2(\eta_0/2)$. Then $v_{\parallel} \equiv \sigma u(\mathbf{x}; E, \mu) = \sigma \hat{u}[y - \sin^2(\eta_0/2)]^{1/2}$, where $\sigma \equiv v_{\parallel}/|v_{\parallel}|$, $\hat{u} \equiv 2(\delta\mu B_0/M)^{1/2}$, and we define helical well-depth parameter $y \equiv (E - e\Phi - \mu B_t)/(2\delta\mu B_0)$, equal to 0 for deeply-trapped particles, unity for particles at the $\tau = h/t$ boundary, and $y > 1$ for particles with $\tau = t, p$. With this expression for v_{\parallel} , one has³⁰ $J_b(\psi, \theta; E, \mu) = \hat{J}A(y)$, with $\hat{J} \equiv M\hat{u}L_h$, $L_h \equiv d\ell/d\eta$, equal to $(2\pi)^{-1}$ times the distance across a ripple well, and

$$A(y) \equiv \oint \frac{d\eta}{2\pi} [y - \sin^2(\eta_0/2)]^{1/2} = \frac{4}{\pi} [E(y^{1/2}) - (1-y)K(y^{1/2})]. \quad (9)$$

Here, K and E are the complete elliptic integrals of the first and second kind.

For the comparisons following, we will also need the bounce-averaged Lorentz

operator \bar{C}_L . From Eq.(2), one finds³⁰

$$\bar{C}_L f = \frac{\nu_h}{A'} (\partial_y A \partial_y f), \quad (10)$$

with $\nu_h \equiv \nu/(2\delta)$, and $A'(y) \equiv dA/dy = (2/\pi)K(y^{1/2})$.

Explicitly performing the summation $\sum_{\mathbf{m}}$ over modes in Eq.(8) with the parameters used for the numerical runs, in Fig. 7 is shown the analytic prediction for D^{rr} , D^{EE} , and D^{JJ} for the same α_ω scan shown earlier, for a range of individual launch-values of well-depth y . Used here is spectrum S2, and $\alpha_E = 0.6$. D^{EE} and D^{JJ} are in code units. The same plot but with $\alpha_E = 0.0$ looks almost the same, but is symmetric about $\alpha_\omega = 0$, *i.e.*, turning on α_E has the effect, through $\dot{\eta}_d \neq 0$, of shifting the analytic D 's to the left, consistent with the numerical shift seen in Fig. 6 in turning on α_E , most evident there in the narrow central tokamak peak, already discussed. The general form of the $D^{EE, JJ}$ curves in Fig. 7 can be understood as follows. Each mode gives a qualitatively similar contribution, but with the lower-frequency modes contributing at larger values of $|\alpha_\omega|$, in order that $\omega_{\mathbf{m}}$ in $\bar{l}_b \propto (\omega_{\mathbf{m}} - \dot{\eta}_d)$ be the same. For each mode \mathbf{m} , the contributing value of $|\bar{l}_b|$ also increases as $|\alpha_\omega|$ does. Since both \bar{l}_b and $\omega_{\mathbf{m}}$ vanish near $\alpha_\omega = 0$, both $D^{JJ} \sim \bar{l}_b^2$ and $D^{EE} \sim \omega_{\mathbf{m}}^2$ vanish there, with the quadratic form seen. For $|\alpha_\omega|$ large enough that $\bar{l}_b > z_b$, the factor $J_{\bar{l}_b}^2$ causes the D 's to fall off rapidly.

Fig. 8 shows the same analytic theory, but now for spectrum S1. All 3 D 's are similar in form to their counterparts for spectrum S2 in Fig. 7. However, while D^{rr} is also comparable to Fig. 7 in magnitude, D^{EE} in Fig. 8 is smaller by a factor of about 2, and D^{JJ} is smaller by a factor of about 25. Since D^{JJ} is dominantly responsible for the pitch-angle scattering yielding ν_{an} , one expects a much smaller ν_{ef} effect from spectrum S1, as observed in Fig. 6. This smaller magnitude is because for $z_b \lesssim 1$, as is the case here, $D^{JJ} \sim J_1^2(z_b) \simeq z_b^2/4 \sim k_{\parallel}^2$. The relative ineffectiveness of turbulence with $k_{\parallel} \ll k$ in producing velocity-space

versus radial changes has been noted earlier^{31,32,29} in a tokamak context.

A comparison of these analytic expressions with numerical runs is shown in Fig. 9, for spectrum S2, $\alpha_E = 0.6$, as in Fig. 7, for a single initial well-depth $y = 0.15$, and a single initial $\theta = 0.3\pi$. One sees the central tokamak peak in both D^{rr} and D^{EE} , but not in D^{JJ} . This is because of the difference discussed above in the way D^{JJ} is computed — only $\tau = h$ particles contribute to it, while as noted earlier, the tokamak peak is due to untrapped particles. Removing these peaks, one sees semiquantitative agreement between the analytic and numerical $D^{EE,JJ}$ curves, rising from a small value near $\alpha_\omega = 0$, shifted due to $\dot{\eta}_d \neq 0$ as noted, and starting to fall off at large $|\alpha_\omega|$. A local smoothing over α_ω of the numerical values yields still better agreement. The local (in α_ω) disparities are unsurprising, due to sources of error noted above in both the analytic and numerical results.

The analytic and numerical D^{rr} curves in Fig. 9, however, do not agree. Removing the tokamak peak from the numerical curve, the analytic D^{rr} is small compared with the numerical curve, and different in α_ω -dependence. We attribute this to the fact, noted in Sec. IV, that the analytic D^{rr} only captures the direct portion of radial transport, and not the indirect portion due to ν_{ef} , which here is dominant, and whose form should resemble the velocity-related coefficients $D^{EE,JJ}$, as it does.

Finally, we assess the size of ν_{an} from these collisionless results in comparison with ν . Since it is D^{JJ} which mainly affects pitch-angle scattering, one has $\nu_{an}/\nu \simeq D_{an}^{JJ}/D_{nc}^{JJ}$. Both D_{an}^{JJ} and D_{nc}^{JJ} may be computed numerically or theoretically, as already displayed for D_{an}^{JJ} in the comparison in Fig. 9. The theoretical value $D_{nc,th}^{JJ}$ of D_{nc}^{JJ} may be obtained using Eq.(10). One finds $D_{nc,th}^{JJ} = \frac{1}{2}d_t\langle(\delta J_b)^2\rangle \simeq \frac{1}{2}\hat{J}^2 d_t\langle(\delta y)^2\rangle \simeq \nu_h \hat{J}^2 A/A'$. For particles with $y = 0.15$, this yields $D_{nc,th}^{JJ} = 2.02 \times 10^{-13}$, compared with the numerical value $D_{nc,num}^{JJ} =$

0.72×10^{-13} from ORBIT. As noted earlier in connection with Fig. 9, several sources of inaccuracy, especially in the numerical computation of D^{JJ} , could produce this disparity, a factor of about 2.8.

Assuming, as is the case for the α_ω -scan for $\alpha_E = 0$ in Fig. 6, that the particles are in the $1/\nu$ regime, one has $D(\nu, \alpha_A = 0) = D_{nc} \propto 1/\nu$. Assuming the effect of turning on the spectrum is simply to replace ν by $\nu_{ef} = \nu + \nu_{an}$ in this expression, one expects $D(\nu, \alpha_A)/D_{nc} \simeq 1/(1 + \nu_{an}/\nu) \simeq 1/(1 + D_{an}^{JJ}/D_{nc}^{JJ})$. In Fig. 10a we plot the theoretically-evaluated factor on the right side of this equation, for a set of values of y , with D_{an}^{JJ} drawn from the curves in Fig. 7. D_{an}^{JJ} and D_{nc}^{JJ} have a similar y -dependence, and as a result their ratio is only weakly dependent on y . In Fig. 10b we plot the value on the left side of that equation, drawn from the numerical results in Figs. 5 and 6. One notes that the analytic theory represents well the variation of the numerical curve. The latter shows some additional finer-scale oscillations, including the central tokamak feature, which have approximately the same periodicity as those noted for CS1 in Fig. 4b. We ascribe these to particles with $\tau = t, p$, not included in the present theory. Those with $\tau = p$ can have larger transit frequencies across the perturbations, and thus their resonance condition has a shorter periodicity in α_ω .

VI. Discussion

We have seen that fluctuations can induce an appreciable anomalous collisionality ν_{an} , and thereby modify the radial transport, consistent with the ν_{ef} intuition. The effect is larger for larger stellarator ripple, and for perturbations having larger k_{\parallel}/k . For a conventional stellarator such as CS1, at fluctuation levels $e\phi/T \sim .01$ characteristic of drift turbulence, the modification of ν_{ef} and of the radial transport coefficients D can be an order unity effect for spectra like S2 with $k_{\parallel} \sim k$, con-

sistent with what was found experimentally in Ref. 19. For spectra with $k_{\parallel} \ll k$, such as in the simple model S1 of drift turbulence, the effect is smaller, around the 10% level for stellarators like CS1. Since $D^{JJ} \sim z_b^2$ for small z_b , this effect might be somewhat larger for a spectrum with larger $\langle k \rho_g \rangle$ than used here. The effect is smaller even for an S2-like spectrum for stellarators like QA1, designed to have small ripple, so that one would expect neither turbulence nor externally-applied fluctuations to have an appreciable impact for these.

We also have seen that the fluctuations produce radial transport by 2 general mechanisms, directly, by inducing extra radial drifts, and also indirectly, via modifications by ν_{an} of the velocity-space dependence of the distribution function f . The indirect effect is most significant for ripple-trapped particles, while the direct effect is captured by typical theories of drift turbulence in tokamaks, due mainly to non ripple-trapped particles, and contributes in stellarators as well.

While one expects the indirect effect to be small for QA and quasi-helical (QH) stellarators, conventional stellarators and those using the “quasi-omnigenous”(QO) or “quasi-isodynamic”(QI) approach to transport optimization,^{33–35} such as the Wendelstein 7-X (W7-X) stellarator³⁶ now under construction, have appreciable ripple. Moreover, the considerable curvature and twisting present in stellarator shapes produces much greater coupling among harmonics (m, n) in an eigenmode than in tokamak eigenmodes,³⁷ which may invalidate the small- k_{\parallel} assumption used in the simple drift model S1. In W7-X, such distortion is especially large near the sharp bends at the corners of the device’s pentagonal shape, just where marginally-trapped particles, the dominant contributors to $1/\nu$ transport in a QO device, have their turning points. For such devices, therefore, the ν_{ef} effect addressed here may be significant.

The fluctuation spectrum has a species dependence, and therefore will have

an effect on the ambipolarity condition determining the radial field $E_r(\psi)$. If the spectrum has typical frequencies $\omega \sim \Omega_{bi}$, as is the case for ITG turbulence, ν_{an} will be appreciable for ions but not electrons, while if instead $\omega \sim \Omega_{be}$, as occurs for ETG turbulence, electrons but not ions would be affected. The effect of this on the fluxes depends on at which root³⁸ of the ambipolarity condition the plasma is. For a plasma at the ion root, the ions are typically in the superbanana regime of Fig. 5, while electrons, typically in the $1/\nu$ regime, hold the ions in. Fluctuations with $\omega \sim \Omega_{be}$ will tend to reduce the electron (particle and heat) fluxes Γ_e , and thus also reduce the ion fluxes Γ_i , by increasing E_r at the radius in question. (See Ref. 38 for a diagrammatic means of understanding this.) This is the basis for the confinement enhancement observed in Ref. 19. On the other hand, since Γ_e is insensitive to E_r , fluctuations with $\omega \sim \Omega_{bi}$ will enhance $|E_r|$, but will leave the fluxes approximately unchanged. At the electron root, for parameters like those used in Ref. 38, fluctuations with $\omega \sim \Omega_{be}$ will increase Γ_e and Γ_i , decreasing the ambipolar value of E_r , while those with $\omega \sim \Omega_{bi}$ will have the opposite effect. In addition, there is the potential for jumping from one root to another within the plasma column, which can generate a transport barrier.³⁹ Such jumps can be induced even by small changes in the fluxes, and thus, the modifications to transport discussed here may be significant, and may be intentionally manipulated by an externally-imposed spectrum.

Finally, at high plasma β , the perturbing modes will acquire a significant magnetic component. Essentially the same analysis as in Sec. IV applies for such magnetic perturbations, but with modified expressions for $h(\mathbf{z}), h_{\mathbf{lm}}$, which have a stronger energy scaling: $h_{\mathbf{lm}} \sim E^0$ for ES perturbations, $\sim E^{1/2}$ for magnetic “braiding”, and $\sim E$ for perturbations of the magnetic ripple.^{29,40} While the ν_{ef} effect from ES fluctuations is thus negligible for energetic ions, the magnetic coun-

terpart could be significant.

Acknowledgments

The authors are grateful to J. Nührenberg and R.B. White for useful discussions.

This work supported by U.S.Department of Energy Contract No.DE-AC02-76-CHO3073.

References

- ¹A.A. Galeev, R.Z. Sagdeev, *Sov.Phys–JETP* **26**, 233 (1968).
- ²F.L. Hinton, R.D. Hazeltine, *Rev. Mod. Phys* **48**,Part 1, 239 (1976).
- ³S.P. Hirshman, D.J. Sigmar, *Nucl. Fusion* **21**, 1079 (1981).
- ⁴A.A. Galeev,R.Z. Sagdeev, *Rev. Plas. Physics*, edited by M.A. Leontovich (Consultants Bureau, New York 1979), Vol.7, p.257.
- ⁵L.M. Kovrizhnykh, *Physica Scripta* **43**, 194 (1984).
- ⁶W.Horton, *Rev. Modern Physics* , 735 (1999).
- ⁷B. Scott, *Phys. Plasmas* **7**, 1845 (2000).
- ⁸A. Kendl, B.D. Scott, H. Wobig, *Plasma Phys. Controlled Fusion* **42**, L23 (2000).
- ⁹F. Jenko, A. Kendl, *Phys. Plasmas* **9**, 4103 (2002).
- ¹⁰G. Rewoldt, L.P. Ku, W.M. Tang, H. Sugama, N. Nakajima, K.Y. Watanabe, S. Murakami, H. Yamada, W.A. Cooper, *Nucl. Fusion* **42**, 1047 (2002).
- ¹¹M,Romé, V. Erckmann, U. Gasparino, N. Karulin, *Plasma Phys, Control. Fusion* **40**, 511 (1998).
- ¹²A.F. Almagri, D.T. Anderson, F.S.B. Anderson, et al. *IEEE Transactions On Plasma Science* **27**, 114 (1999).
- ¹³G.H. Neilson, M.C. Zarnstorff, J.F. Lyon, the NCSX Team, *Journal of Plasma and Fusion Research* **78**, 214-219 (2002).
- ¹⁴D. Mikkelsen, H. Maassberg, M.C. Zarnstorff, C.D. Beidler, *et al.*, (to appear in publication in *Fusion Science & Technology*, 2004).

- ¹⁵U. Stroth, M. Murakami, R.A. Dory, H. Yamada, F. Sano, T. Obiki, *Nucl. Fusion* **36**, 1063 (1996).
- ¹⁶K. Lackner, N.A.O. Gottardi, *NF* 30, p767 (1990).
- ¹⁷M. Dobrowolny, O.P. Pogutse, *Phys. Rev. Lett.* **25**, 1608 (1970).
- ¹⁸P.A. Demirkhanov, M.A. Stotland, Sh.V. Khil', *Sov. Phys. Tech. Phys.* **17**, 1128 (1973).
- ¹⁹V.S. Voitsenya, A.Yu. Voloshko, S.S. Kalinichenko, S.I. Solodovchenko, A.F. Shtan, *Sov.J.Plasma Phys.* **3**, 659 (1977).
- ²⁰O. Motojima, A.A. Shishkin, S. Inagaki, K.Y. Watanabe, *Nucl.Fusion* **40** 833 (2000).
- ²¹A. Shishkin, O. Shyshkin, H. Wobig, Y. Igitkhanov, O. Motojima, S. Morimoto, K. Yamzaki, S. Inagaki, *J. Nucl. Materials* **313**, 1192 (2003).
- ²²O. Antufyev, A. Shishkin, *Fusion Science & Technology* **46**, 1536 (2004).
- ²³R.B. White, M.S. Chance, *Phys. Fluids* **27**, 2455 (1984).
- ²⁴A.H. Boozer, G. Kuo-Petavic, *Phys. Fluids* **24**, 851 (1981).
- ²⁵A.A. Galeev, R.Z. Sagdeev, H.P. Furth, M.N. Rosenbluth, *Phys. Rev. Letters* **22**, 511 (1969).
- ²⁶A.N. Kaufman, *Phys. Fluids* **15**, 1063 (1972).
- ²⁷H.E. Mynick, J.A. Krommes, *Phys. Fluids* **23**, 1229 (1980).
- ²⁸I.B. Bernstein and K. Molvig, *Phys. Fluids* **26**, 1488 (1983).
- ²⁹H.E. Mynick and R.E. Duvall, *Phys. Fluids–B* 1, 750 (1989).

- ³⁰H.E. Mynick, W.N.G. Hitchon, *Nucl. Fusion* **26**, 425 (1986).
- ³¹D. A. Hitchcock, R. D. Hazeltine and S. M. Mahajan, *Phys. Fluids* **26**, 2603 (1983).
- ³²K.C. Shaing, *Phys. Fluids* **31**, 2249 (1988).
- ³³H.E. Mynick, T.K.Chu, A.H.Boozer, *Phys. Rev. Letters* **48**, 322 (1982).
- ³⁴J. Nührenberg, R. Zille, *Phys. Lett.* **114A**, 129 (1986).
- ³⁵S. Gori, W. Lotz, J. Nuehrenberg, Theory of Fusion Plasmas (International School of Plasma Physics), Bologna: SIF (1996), 335.
- ³⁶C. Beidler, G. Grieger, F. Herrnegger, E. Harmeyer, J. Kisslinger, W. Lotz, H. Maassberg, P. Merkel, J. Nuhrenberg, F. Rau, J. Sapper, F. Sardei, R. Scardovelli, A. Schluter H. Wobig, *Fusion Techn.* **17**, 148 (1990).
- ³⁷V. Kornilov, R. Kleiber, R. Hatzky, L. Villard, G. Jost, *Phys. Plasmas* **11**, 3196 (2004).
- ³⁸H.E. Mynick, W.N.G. Hitchon, *Nucl. Fusion* **23**, 1053 (1983).
- ³⁹U. Stroth, K. Itoh, S.-I. Itoh, H. Hartfuss, H. Laqua, the ECRH team, & the W7-AS team, *Phys. Rev. Lett.*, **86**, 5910 (2001).
- ⁴⁰H.E. Mynick, *Phys. Fluids-B* **5** 2460-2467 (1993).

Figures

FIG. 1. Plots of (left) $B(\theta, \zeta)$ over the flux surface at $\psi = \psi_a/2$ and (right) $B(\ell)$ along a field line for one poloidal transit, for each of the 3 configurations studied in the paper: (a)TOK1, (b)QA1, and (c)CS1. The slanting line indicates the pitch of the magnetic field in these flux coordinates.

FIG. 2. Diffusion coefficient $D(\text{cm}^2/\text{sec})$ versus central electron density $n_{e0}(\text{cm}^{-3})$ for spectrum S1, $E_r = 0$, for each of TOK1 (bottom), QA1 (middle), and CS1 (top).

FIG. 3. Scan of diffusion coefficient D versus perturbation amplitude α_A , for $n_{e0} = 10^{13}/\text{cm}^3$, $\alpha_\omega = .03$, and for each of TOK1, QA1, and CS1. (a)Full D value. (b)Anomalous increment D_{an} to D from the curves in (a), equal to D minus the value for $\alpha_A = 0$.

FIG. 4. Scan of diffusion coefficient D versus frequency amplitude α_ω , for TOK1, QA1, and CS1. (a)Full D . (b)Anomalous increment $D_{an} \equiv D - D_{nc}$.

FIG. 5. Scan of D versus density at $\alpha_A = 0$ for configuration CS1, for $\alpha_E = 0$ (upper curve) and $\alpha_E = 0.6$, manifesting both the $1/\nu$ regime at higher n_{e0} , and the superbanana regimes at lower n_{e0} .

FIG. 6. Frequency scan of D for CS1, for (A) $\alpha_E = 0$, spectrum S1, (B) $\alpha_E = 0$, spectrum S2, (C) $\alpha_E = 0.6$, spectrum S1, (D) $\alpha_E = 0.6$, spectrum S2. Fig. 6a shows the full D , Fig. 6b shows the anomalous increment D_{an} .

FIG. 7. Frequency scan of analytic theory for D^{rr} , D^{EE} , and D^{JJ} for a range of well-depth $y < 1$, and for spectrum S2, $\alpha_E = 0.6$. $D^{EE, JJ}$ are in code units.

FIG. 8. Frequency scan of analytic theory as in Fig. 7, but for spectrum S1.

FIG. 9. Comparison of analytic and numerical calculations for spectrum S2, $\alpha_E = 0.6$, as in Fig. 7, for a single launch well-depth $y = 0.15$.

FIG. 10. (a) Frequency scan of theoretical prediction for $1/(1 + \nu_{an}/\nu)$, for indicated values of y . (b) Frequency scan of $D^{rr}(\alpha_A = 10)/D_{nc}$, with data drawn from Figs. 5 and 6.

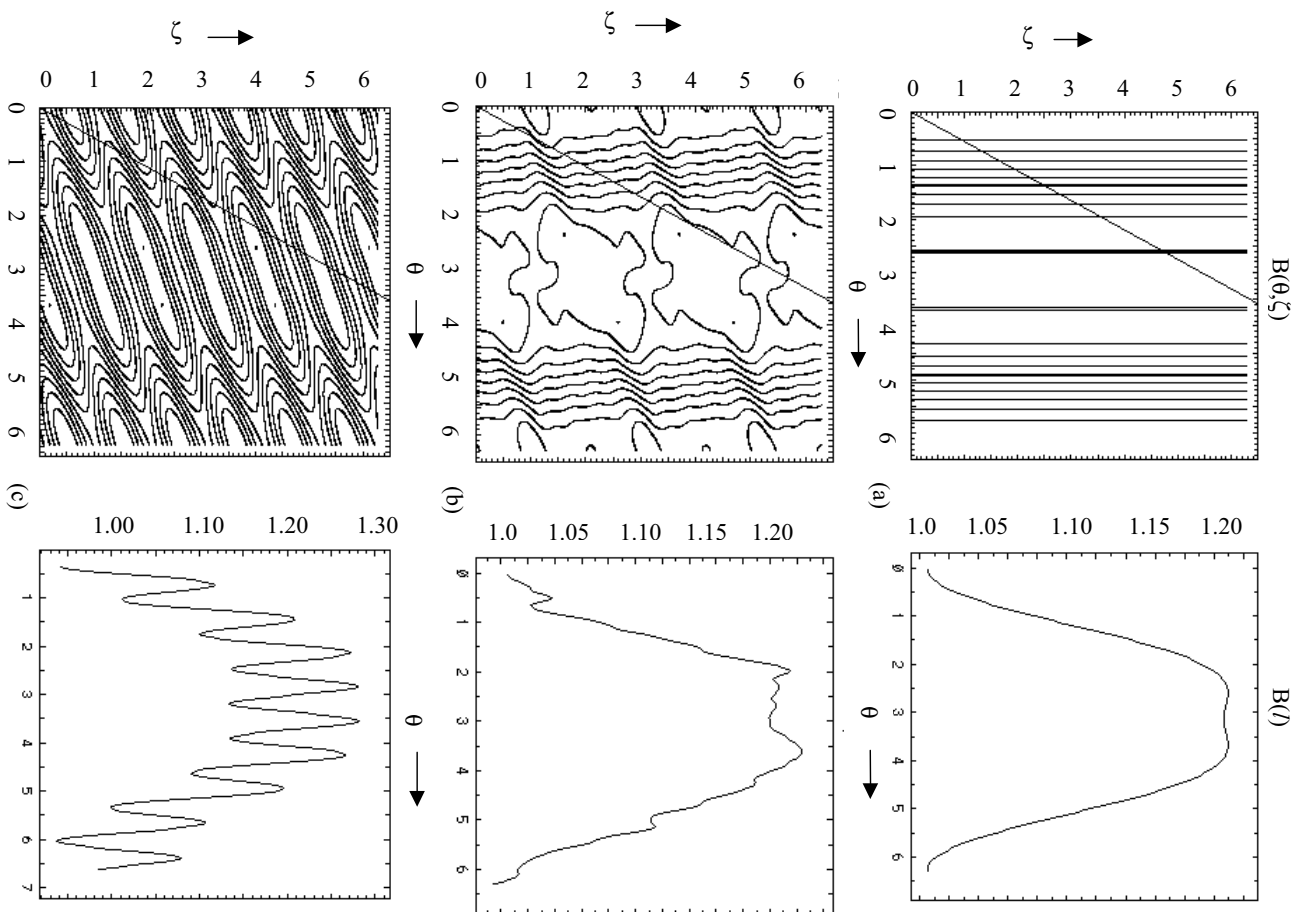


Figure 1:

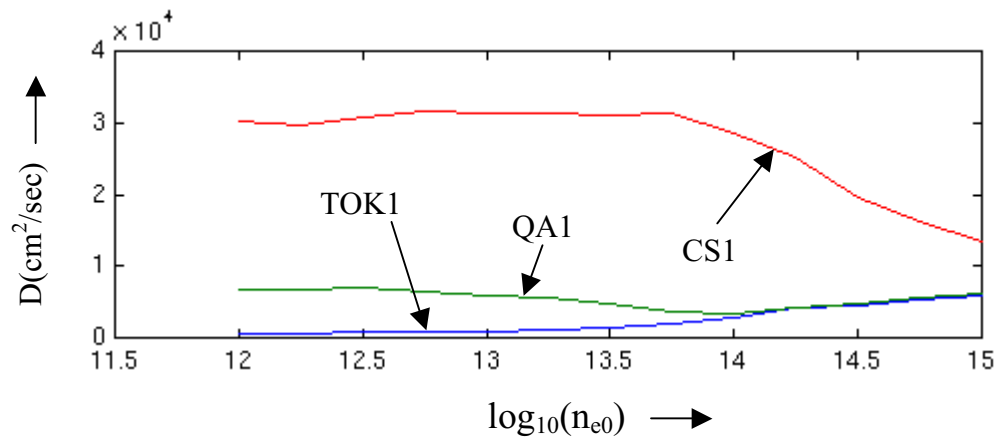


Figure 2:

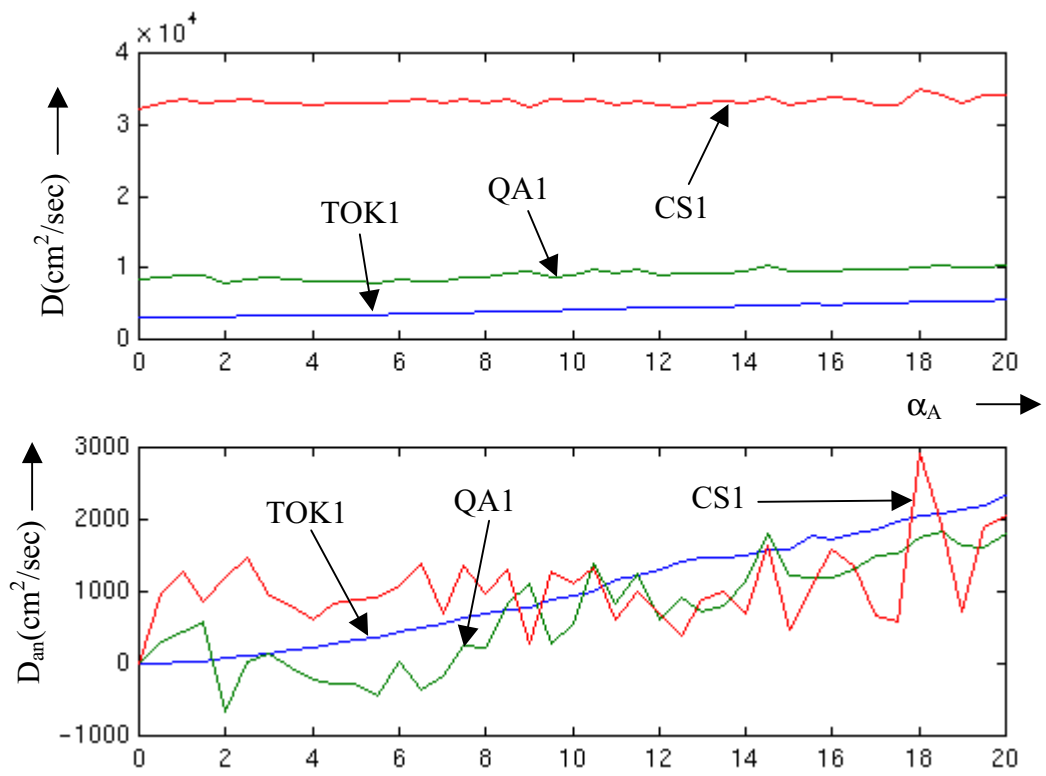


Figure 3:

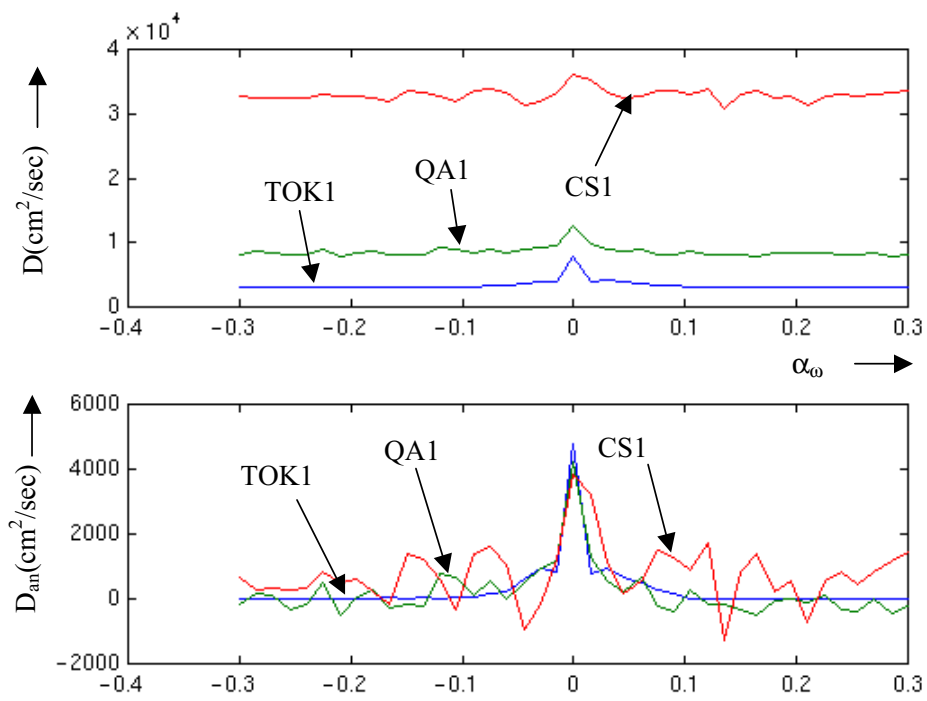


Figure 4:

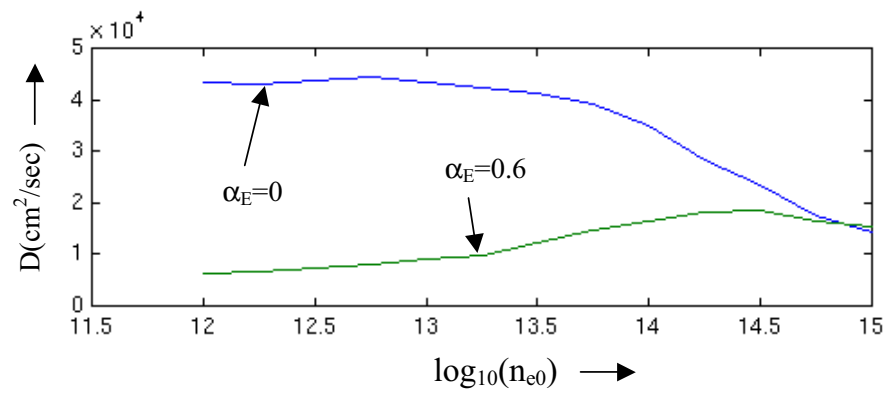


Figure 5:

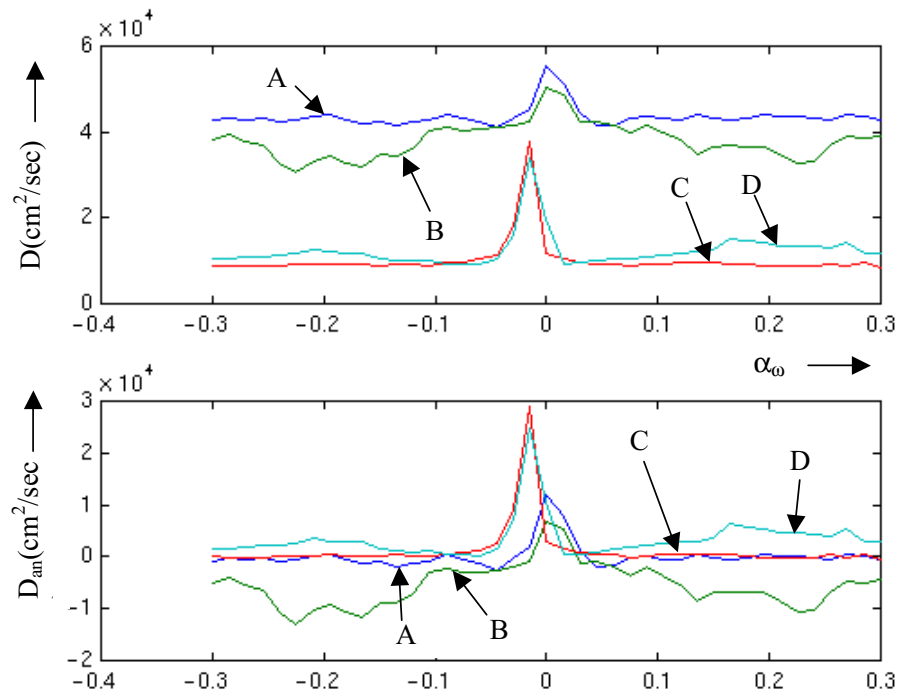


Figure 6:

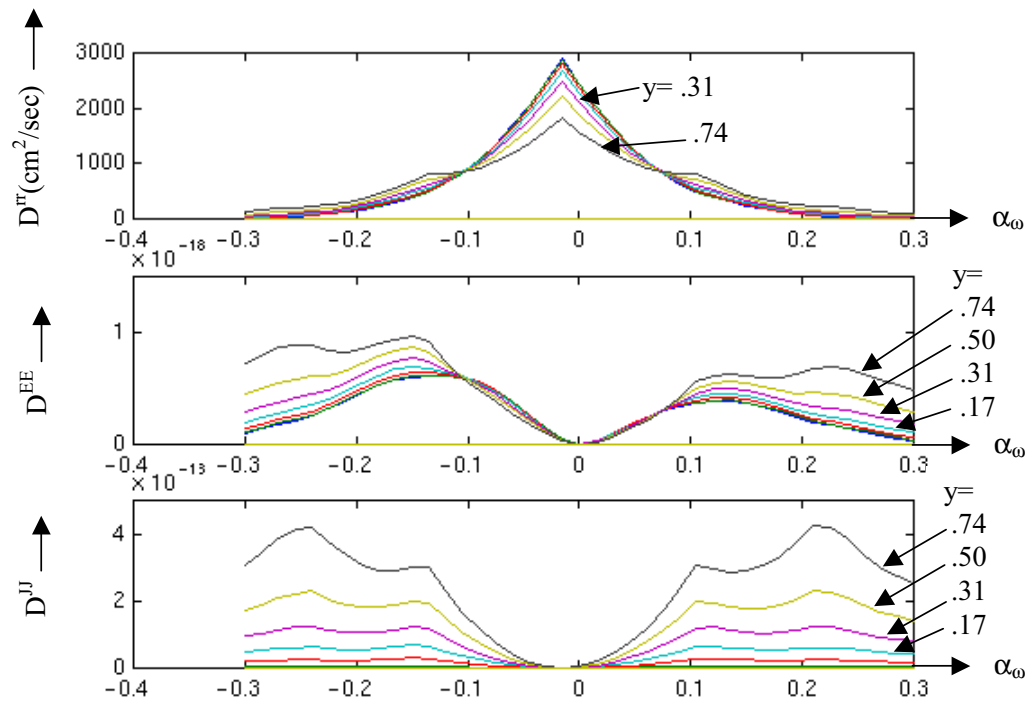


Figure 7:

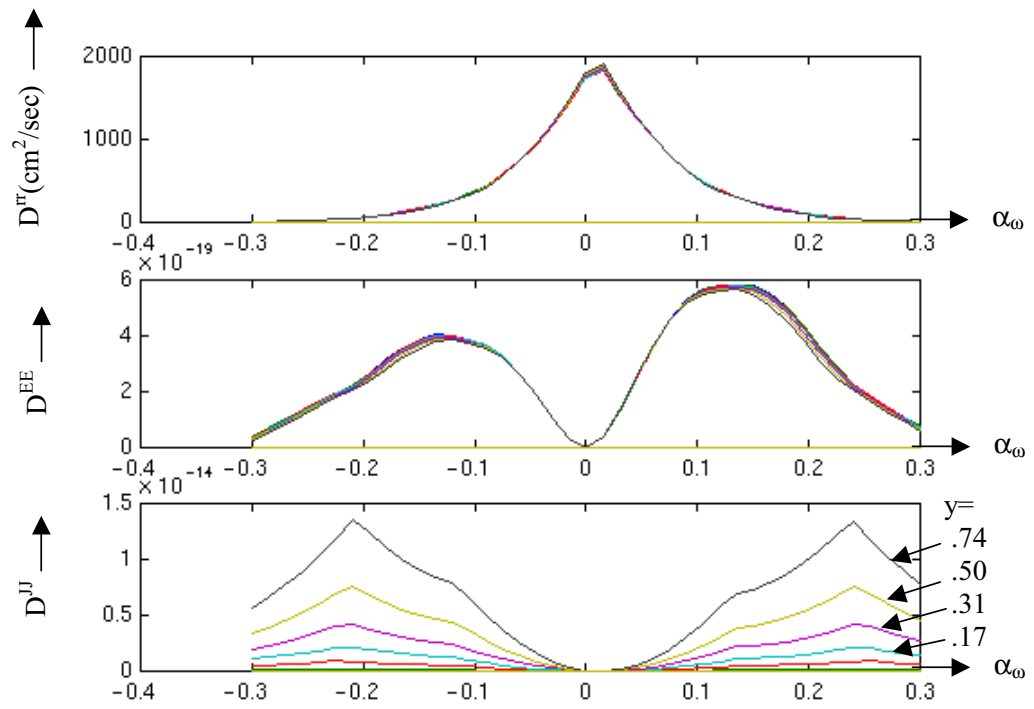


Figure 8:

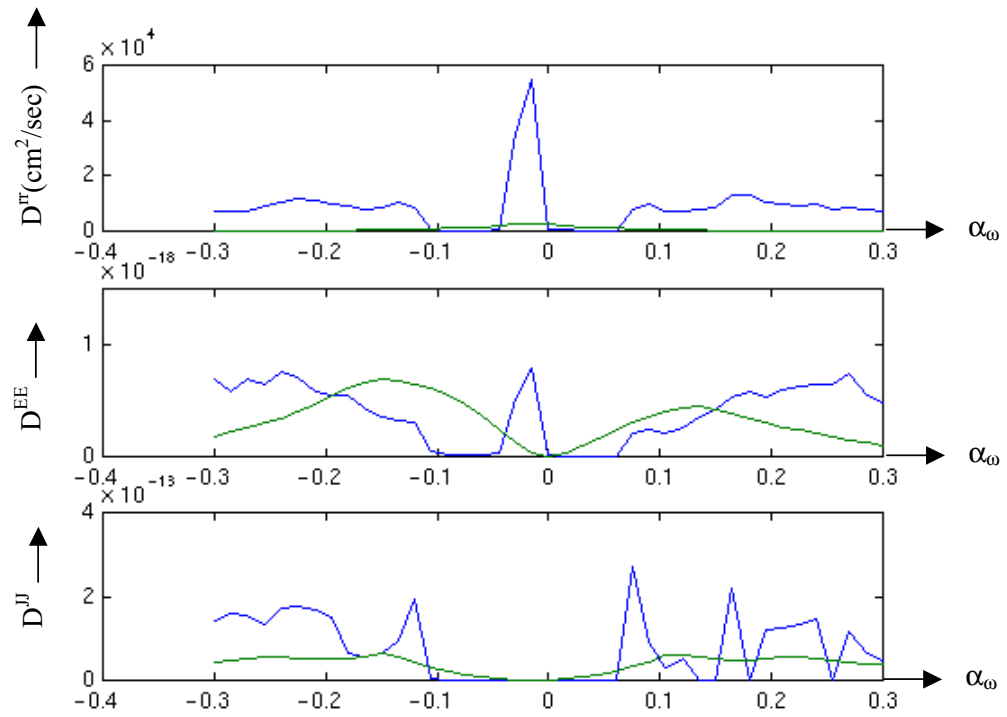


Figure 9:

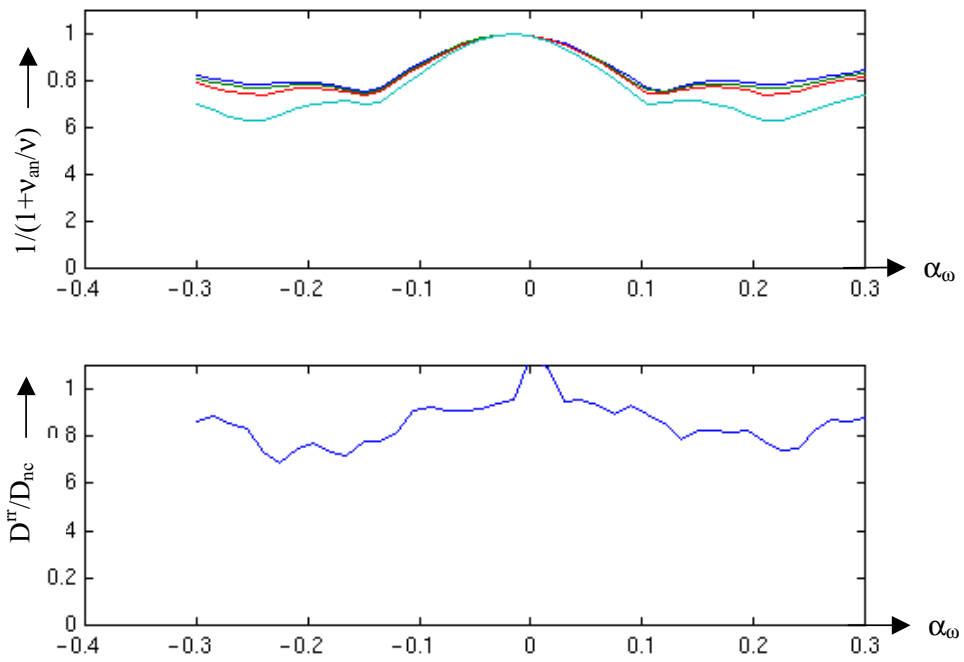


Figure 10:

External Distribution

Plasma Research Laboratory, Australian National University, Australia
Professor I.R. Jones, Flinders University, Australia
Professor João Canalle, Instituto de Fisica DEQ/IF - UERJ, Brazil
Mr. Gerson O. Ludwig, Instituto Nacional de Pesquisas, Brazil
Dr. P.H. Sakanaka, Instituto Fisica, Brazil
The Librarian, Culham Laboratory, England
Mrs. S.A. Hutchinson, JET Library, England
Professor M.N. Bussac, Ecole Polytechnique, France
Librarian, Max-Planck-Institut für Plasmaphysik, Germany
Jolan Moldvai, Reports Library, Hungarian Academy of Sciences, Central Research Institute
for Physics, Hungary
Dr. P. Kaw, Institute for Plasma Research, India
Ms. P.J. Pathak, Librarian, Institute for Plasma Research, India
Ms. Clelia De Palo, Associazione EURATOM-ENEA, Italy
Dr. G. Grosso, Instituto di Fisica del Plasma, Italy
Librarian, Naka Fusion Research Establishment, JAERI, Japan
Library, Laboratory for Complex Energy Processes, Institute for Advanced Study,
Kyoto University, Japan
Research Information Center, National Institute for Fusion Science, Japan
Dr. O. Mitarai, Kyushu Tokai University, Japan
Dr. Jiengang Li, Institute of Plasma Physics, Chinese Academy of Sciences,
People's Republic of China
Professor Yuping Huo, School of Physical Science and Technology, People's Republic of China
Library, Academia Sinica, Institute of Plasma Physics, People's Republic of China
Librarian, Institute of Physics, Chinese Academy of Sciences, People's Republic of China
Dr. S. Mirnov, TRINITI, Troitsk, Russian Federation, Russia
Dr. V.S. Strelkov, Kurchatov Institute, Russian Federation, Russia
Professor Peter Lukac, Katedra Fyziky Plazmy MFF UK, Mlynska dolina F-2,
Komenskeho Univerzita, SK-842 15 Bratislava, Slovakia
Dr. G.S. Lee, Korea Basic Science Institute, South Korea
Institute for Plasma Research, University of Maryland, USA
Librarian, Fusion Energy Division, Oak Ridge National Laboratory, USA
Librarian, Institute of Fusion Studies, University of Texas, USA
Librarian, Magnetic Fusion Program, Lawrence Livermore National Laboratory, USA
Library, General Atomics, USA
Plasma Physics Group, Fusion Energy Research Program, University of California
at San Diego, USA
Plasma Physics Library, Columbia University, USA
Alkesh Punjabi, Center for Fusion Research and Training, Hampton University, USA
Dr. W.M. Stacey, Fusion Research Center, Georgia Institute of Technology, USA
Dr. John Willis, U.S. Department of Energy, Office of Fusion Energy Sciences, USA
Mr. Paul H. Wright, Indianapolis, Indiana, USA

The Princeton Plasma Physics Laboratory is operated
by Princeton University under contract
with the U.S. Department of Energy.

Information Services
Princeton Plasma Physics Laboratory
P.O. Box 451
Princeton, NJ 08543

Phone: 609-243-2750
Fax: 609-243-2751
e-mail: pppl_info@pppl.gov
Internet Address: <http://www.pppl.gov>